REVIEW ARTICLE

Neutron stars

James M. Lattimer

Abstract Neutron stars are laboratories for dense matter and gravitational physics. Observations of neutron stars from sources such as radio pulsars, low-mass X-ray binaries, X-ray bursts and thermally-emitting neutron stars are setting bounds to neutron star masses, radii, rotation rates, temperatures and ages. Mass measurements constrain the equation of state at the highest densities and set firm bounds to the highest possible density of cold matter. Radii constrain the equation of state in the vicinity of the nuclear saturation density and yield information about the density dependence of the nuclear symmetry energy. Laboratory measurements and theoretical studies of pure neutron matter are in remarkable agreement with observational bounds.

1 Introduction

Neutron stars are laboratories for dense matter and gravitational physics, and are among the most extreme environments in the universe. They were first observed in the form of pulsars, which are rapidly rotating, highly magnetized, neutron stars; nearly 2000 pulsars are now known. They are powered by beamed magnetic dipole radiation
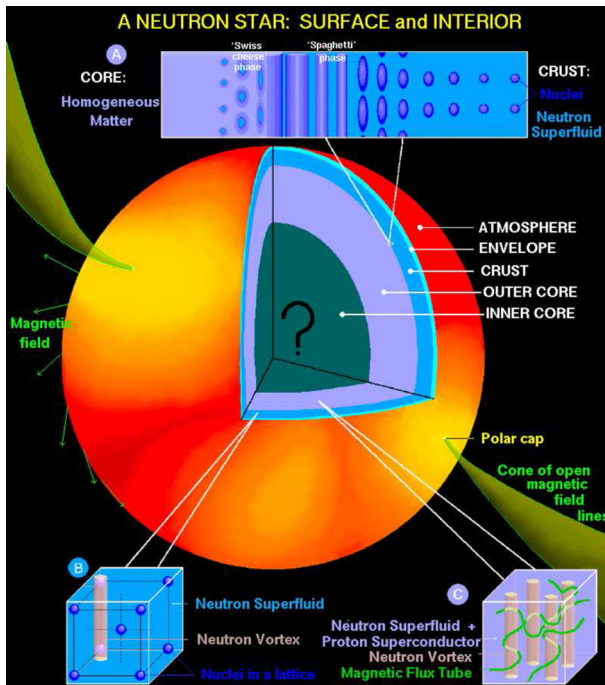

This article belongs to the Topical Collection: The First Century of General Relativity: GR20/Amaldi10.


J. M. Lattimer (✉)
Department of Physics and Astronomy, Stony Brook University, Stony Brook,
NY 11794-3800, USA
e-mail: James.Lattimer@StonyBrook.edu

Fig. 1 This graphic representation of a neutron star illustrates its five significant regions. At the *top*, details of the core-crust boundary is shown. At the *bottom*, possible crustal and core superfluids are illustrated. Beams of energy are directed from the magnetic poles of the star. Figure courtesy of D. Page

stemming from the loss of rotational energy. Neutron stars have also been observed in X-ray binaries through radiation emitted as a consequence of matter accreted from companion stars. A few isolated neutron stars have also been found; many or all of these are pulsars, but the beams are not directed towards the Earth.

In many respects, neutron stars are giant nuclei, with $N \approx 10^{57}$. They can be considered to have five important regions (Fig. 1). The outermost region, or atmosphere, is only about 1 cm thick, but controls the observed spectral energy distribution. To a zeroth order approximation, this distribution is blackbody, but the composition and magnetic field intensity at the surface redistributes the energy. The second layer is the envelope, which acts as a thermal insulator. The effective temperature of the star, for a given age, depends on its composition: stars with hydrogenic atmospheres appear cooler than those with heavy-element envelopes. In these layers, matter consists of a plasma. The mantle is a solid region largely composed of atomic nuclei in a Coulomb lattice. The upper mantle material is similar to that found in white dwarf interiors, with $Z \simeq 56$. Nuclei in the lower mantle, however, have much larger masses and neutron excesses, and are likely deformed. At high-enough density, deformations might become extreme, leading to so-called pasta phases in which spherical nuclei are replaced by rods or plates. At the core-crust boundary, where the density is roughly $\rho_s/3$ with $\rho_s \simeq 3 \times 10^{14} \, \mathrm{g \, cm^{-3}}$ being the nuclear saturation density, the inhomogeneous phase with nuclei gives way to a homogeneous phase of nucleons in the outer
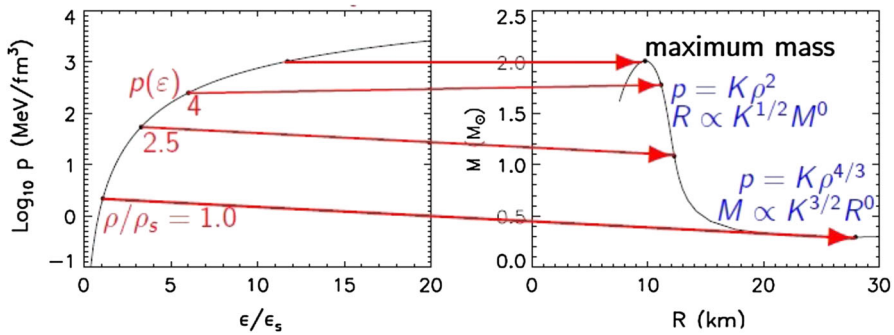
Fig. 2 Integration of the TOV equations with an EOS (*left panel*), beginning from different central densities and pressures, leads to the $M - R$ curve (*right panel*). The EOS displayed leads to a maximum neutron star mass of about $2 : 05 M_\odot$ and the radius of a $1.4 M_\odot$ star is about 12 km. The *four arrows* show the $M - R$ resulting from the indicated central densities. At low densities, the pressure scales with $\rho^{4/3}$; in Newtonian gravity this implies M is independent of R. At high densities, $p \propto \rho^2$, leading to R being nearly independent of M. $1.4 M_\odot$ stars typically have central densities in the range $2 - 3\rho_s$. Figure adapted from Ref. [1]

core. The matter is charge-neutral, so the number of protons and electrons are equal. For $\rho > \rho_s$, muons in addition appear. The composition of the inner core is largely unknown: it could range from an extension of the outer core and be primarily nucleonic, or be a mixture of nucleons and strange matter in the form of hyperons, a Bose condensate, or deconfined quarks. In extreme cases, nucleons may entirely give way to deconfined quarks at the center, although this now appears to be unlikely.

Fortunately, details of the composition do not affect the overall structure of the star, which is controlled by the Tolman–Oppenheimer–Volkov (TOV) stellar structure equations from general relativity:

$$\frac{dp}{dr} = -\frac{G}{c^4} \frac{(Mc^2 + 4\pi p r^3)(\varepsilon + p)}{r(r - 2GM/c^2)}, \qquad \frac{dm}{dr} = 4\pi \varepsilon r^2 / c^2, \tag{1}$$

where p is the pressure, $\varepsilon = \rho c^2$ is the energy density, and m is the gravitational mass interior to the radius r. These equations have boundary conditions: For $r = 0$, all radial gradients and m are zero. $p = 0$ at the surface where $r = R$ and $m = M$. Therefore, a given equation of state, which specifies $p(\epsilon)$, dictates a unique mass-radius $M - R$ curve (Fig. 2).

A number of general features can be gleaned from Fig. 2. First, it is a consequence of general relativity that a maximum mass exists for any causal equation of state (EOS). (Causality is the condition that the isothermal speed of sound $\sqrt{dp/d\rho}$ never exceeds the speed of light.) In Newtonian gravity, there is no maximum mass. Second, the nature of the equation of state dictates the slope of the $M - R$ curve. This can be seen from dimensional analysis of the structure equations, ignoring the general relativistic terms. If the EOS is dominated by a polytropic law $p = K\rho^\gamma$, dimensional analysis gives

$$M \propto K^{1/(2-\gamma)} R^{(4-3\gamma)/(2-\gamma)}. \tag{2}$$

Since the pressure at low densities is dominated by electron degeneracy pressure, $p \propto \rho^{4/3}$ and $M \propto R^0$, so the $M - R$ curve is flat for small masses. On the other hand, nearly all theories for dense matter suggest that $\gamma \approx 2$, so intermediate-mass stars have vertical $M - R$ trajectories with R being independent of the mass. What controls the value of the radius is K in the pressure-density law. Third, the typical neutron star mass, $1.4M_\odot$, is characterized by a central density of $2 - 3\rho_s$ so that the average density is nearly ρ_s. This strongly suggests that the value of K in the vicinity of ρ_s is fundamentally related to the typical neutron star radius – which we show to be true below. This is extremely important, because it suggests that determination of neutron star radii is well within the realm of both nuclear structure and neutron matter studies.
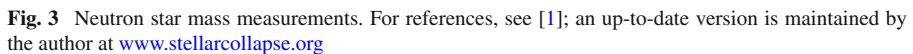
Meanwhile, an astrophysics goal is to invert the TOV equations and use M and R measurements to delineate the underlying $p - \varepsilon$ relation. We will focus on some of the more relevant, recent observations and their interpretation, including the measurements of the masses of pulsars and neutron stars in X-ray binaries, and estimates of neutron star masses and radii in photospheric radius expansion X-ray bursts and quiescent low-mass X-ray binaries. These observations will be interpreted in terms of their underlying nuclear physics and related to nuclear experimental results concerning nuclear binding energies, flows in heavy ion collisions, neutron skin thicknesses, dipole polarizabilities and giant dipole resonances. In addition, they will be compared to results inferred from recent theoretical studies of the properties of pure neutron matter.
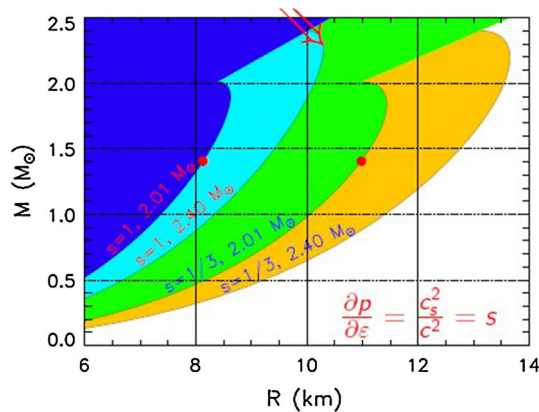
Observations of cooling neutron stars up to a million years old also shed light on their internal compositions. Recent observations of Cas A seem to even pinpoint the critical temperature of a core neutron superfluid [2,3]. It is outside the scope of this contribution, however, to discuss cooling, but a comprehensive cooling study could possible restrict masses and radii. Multiple other methods of estimating radii will be discussed briefly in the conclusions.

2 Extremal properties of neutron stars

The most accurate neutron star measurements concerns their masses. About 40 neutron star masses have been measured with reasonable, and in some cases, extraordinary precision (see [1] for a review). The author maintains a regularly updated database of mass measurements at www.stellarcollapse.org, and Fig. 3 summarizes measurements.The most interesting feature of the mass measurements is the largest well-measured neutron star mass. Currently, from measurements of PSR J1614+2230 [4], with $M = 1.97 \pm 0.04M_\odot$, and PSR J0348+0432 [5], with $M = 2.01 \pm 0.04M_\odot$, the minimum value of the maximum mass is $\hat{M} = 2M_\odot$. Obviously, this contains important information about the high-density EOS. However, it also sets interesting limits on properties of the equation of state at lower densities and on the radii of intermediate-mass neutron stars, as we now show.

Koranda, Stergioulas and Friedman [6] hypothesized that the most compact stellar configurations occur when the EOS has a 'maximally compact' form, $p = \varepsilon - \varepsilon_0$. This ensures at low densities, the pressure is as soft as possible (i.e., $p = 0$), and at high densities, the pressure is as stiff as possible (i.e., causal). With this EOS, the TOV

Fig. 3 Neutron star mass measurements. For references, see [1]; an up-to-date version is maintained by the author at www.stellarcollapse.org

equations can be reduced to a dimensionless form with a single EOS scale parameter, ε_0. Define the dimensionless variables

$$w = \epsilon/\varepsilon_0, \quad y = p/\varepsilon_0, \quad x = r\sqrt{G\varepsilon_0}/c^2, \quad z = m\sqrt{G^3\varepsilon_0}/c^2. \quad (3)$$

The maximum mass configuration is achieved when $w_c = 3.034, x_R = 0.2404$, $y_c = 2.034, z_R = 0.08513$ (c and R denote the center and surface, respectively). A useful scale is the nuclear saturation density $\rho_s = 2.7 \times 10^{14}\,\mathrm{g\,cm^{-3}}, n_s = 0.16$ baryons $\mathrm{fm^{-3}}$, or $\varepsilon_s = 150\,\mathrm{MeV\,fm^{-3}}$. Then the maximum neutron star mass is $M_{\mathrm{max}} = 4.1\sqrt{\varepsilon_s/\varepsilon_0}M_\odot$, which reproduces the well-known Rhoades and Ruffini result [7]. One also finds the maximum compactness condition, in the form of a minimum radius $R_{\mathrm{min}} = 2.82\,GM/c^2$ km for mass M, which was previously anticipated by Glendenning [8,9]. Furthermore, this also establishes the conjecture of Lattimer and

Fig. 4 The *dark blue* region shows the $M - R$ region forbidden by the observed value $\hat{M} = 2.01 M_\odot$, and is a combination of the maximally compact $M - R$ (*arrow*) and R_{min} curves. The *light blue* region illustrates the region forbidden by a hypothetical value of $\hat{M} = 2.4 M_\odot$. The last two regions have the same interpretation, but for a maximally compact strange quark matter EOS $p = (\epsilon - \epsilon_0)/3$ and a rescaled R_{min} curve. Figure adapted from Ref. [1] (color figure online)

Prakash [10] that the maximum central density of any neutron star is determined from the largest measured mass $\hat{M}$:

$$\epsilon_{c,max} = 3.034\varepsilon_0 \simeq 51(M_\odot/\hat{M})^2\varepsilon_s. \tag{4}$$

Paradoxically, this relation implies that the larger is $\hat{M}$, the smaller will be the maximum central density.

The radius limits now set by the largest measured mass can be observed by plotting the $M - R$ curve of the maximally compact EOS, with its maximum mass scaled to the value of the largest measured mass (Fig. 4). Thus, at present, it is seen that a $1.4 M_\odot$ star cannot have a radius smaller than about 8.15 km (left red dot in Fig. 4). If a $2.4 M_\odot$ neutron star were to observed, this radius limit increases to 9.25 km (right red dot). Lattimer and Prakash [10] have been able to demonstrate that models of neutron stars with significant amounts of quark matter in their interiors obey a compactness constraint that is instead given by the EOS of the simple MIT Bag Model $p = (\varepsilon - \varepsilon_0)/3$, which has a similar dimensionless TOV solution, but with less compactness [11]. In this case, if deconfined quark matter exists in a neutron star interior, either in a pure or mixed state with hadrons, a $1.4 M_\odot$ star cannot be smaller than about 11 km. This value is dangerously close to observed values, as we discuss below. Therefore, it appears relatively unlikely that intermediate-mass neutron stars have deconfined quark matter in their interiors.

3 The radius–pressure correlation

Lattimer and Prakash [9] discovered that neutron star radii are highly correlated with the pressure of neutron star matter in the vicinity of ρ_s. Eq. (2) predicts the correlation
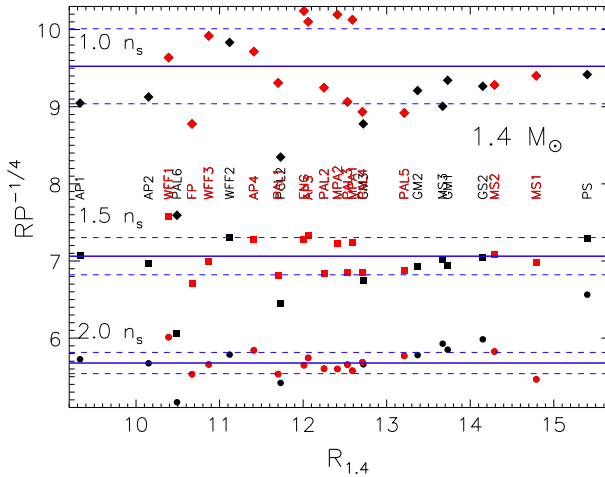
Fig. 5 The phenomenological correlation between neutron star radii and the pressure of neutron star matter in the vicinity of n_s. P represents the pressure at the indicated density. The *red* (*black*) *symbols* represent EOSs which do (not) support a maximum mass of $2M_\odot$. *Diamonds*, *squares* and *circles* represent densities of $2n_s$, $1.5n_s$ and n_s, respectively. *Solid* (*dashed*) *lines* indicate averages (1σ upper and lower limits). The EOS acronyms and figure adapted from Ref. [9] (color figure online)

Table 1 Coefficients $C(n, 1.4M_\odot)$, in km, for the pressure-radius correlation. $\hat{M}$ is the minimum value for the maximum neutron star mass	$\hat{M}/M_\odot$	n_s	$1.5n_s$	$2n_s$
	1.4	9.30 ± 0.58	6.99 ± 0.30	5.72 ± 0.25
	2.0	9.52 ± 0.49	7.06 ± 0.24	5.68 ± 0.14

to be of the form $R \propto \sqrt{p}$, but due to general relativistic effects, the phenomenological relationship is approximately $R \propto p^{1/4}$ (Fig. 5).

This relation can be expressed as

$$R_M = C(n, M)[p_\beta(n)/\text{MeV fm}^{-3}]^{1/4}, \qquad (5)$$

where R_M is the radius of a star of mass M and C are coefficients that depend on the density and mass. The upper row in Table 1 lists $C(n, 1.4M_\odot)$ compiled from about 3 dozen equations of state for three densities. Lattimer and Lim [12] re-analyzed this relation with EOSs restricted to ones which satisfy $\hat{M} = 2.0M_\odot$. Although $C(n, M)$ becomes more accurate at higher densities, p_β can be expressed relatively model-independently in terms of S_v and L only for $n = n_s$ (see Eq. (10) below). Thus, we can only usefully employ $C(n_s, 1.4M_\odot)$ to relate neutron star radii to symmetry energy parameters.

The pressure of neutron star matter near ρ_s is mostly determined by the nuclear symmetry energy. At densities below about $\rho_s/3$, the pressure is primarily due to relativistic degenerate electrons. At higher densities, nuclei dissolve, and the pressure becomes increasingly due to interacting non-relativistic baryons. Symmetric matter, with a proton fraction $x = 1/2$, has zero baryonic pressure at ρ_s. However, neutron star

matter is in β-equilibrium with $x \ll 1/2$: the energy at a minimum with respect to x, which results in the β-equilibrium condition $\mu_n - \mu_p = \mu_e$. It is usual to approximate the x dependence of the baryonic energy as a truncated quadratic expansion:

$$E(n, x) \simeq E(n, 1/2) + S_2(n)(1 - 2x)^2, \tag{6}$$

where the expansion coefficient S_2 is closely related to the nuclear symmetry energy defined by $S(n) = E(n, 0) - E(n, 1/2)$. It is also conventional to expand the coefficient S_2 in a Taylor series in density:

$$S_2(n) \simeq S_v + L(n - n_s)/(3n_s) + \cdots \tag{7}$$

where $S_v \simeq 31$ MeV and $L \simeq 50$ MeV as we argue below from nuclear systematics and astrophysical observations. In the quadratic approximation, the properties of pure neutron matter at n_s are easily determined:

$$E(n_s, 0) \simeq S_v + E(n_s, 1/2) \equiv S_v - B, \qquad p(n_s, 0) \simeq Ln_s/3, \tag{8}$$

where $B \simeq -16$ MeV is the bulk binding energy of symmetric matter at n_s. For neutron star matter in β equilibrium, the proton fraction at n_s is small:

$$x_\beta \simeq (4S_v/\hbar c)^3 (3\pi^2 n_s)^{-1} \simeq 0.04. \tag{9}$$

The pressure at n_s in β-equilibrium is, to second order,

$$p(n_s, x_\beta) \simeq \frac{Ln_s}{3}\left[1 - \left(\frac{4S_v}{\hbar c}\right)^3 \frac{4 - 3S_v/L}{3\pi^2 n_s}\right]. \tag{10}$$

Before examining astrophysical constraints on radii, we examine nuclear physics constraints on the values of S_v and L.

4 Nuclear physics constraints

The symmetry energy changes nucleon distributions in the nucleus, which affects the energy and oscillation modes. The liquid drop model envisions the energy as being primarily due to volume, surface and Coulomb contributions. A transparent way of establishing the liquid droplet model and also visualizing how nuclear observables such as binding energies, dipole resonance energies and neutron skin thicknesses depend on the nuclear force, including its symmetry parameters, is through the nuclear hydrodynamical model proposed by Lipparini and Stringari [13] and generalized by Lattimer and Steiner [14].

4.1 The hydrodynamical model of nuclei

We begin with a simplified Hamiltonian energy density consisting of uniform matter, Coulomb and gradient contributions. Using $n = n_n + n_p$ for the isoscalar density and $\alpha = n_n - n_p$ for the isovector density, we have

$$\mathcal{H} = \mathcal{H}_B(n, \alpha) + n_p V_C/2 + \mathcal{Q}(n)\left(n'\right)^2,$$
$$\mathcal{H}_B(n, \alpha) = \mathcal{H}_B(n, 0) + S_2(n)\alpha^2/n \tag{11}$$

where the uniform matter contribution is $\mathcal{H}_B(n, \alpha)$, V_C is the Coulomb potential, and $\mathcal{Q}(n)$ controls the gradient contributions. If the protons are uniformly distributed for $r < R$,

$$V_C = \frac{Ze^2}{R}\left(\frac{3}{2} - \frac{r^2}{2R^2}\right) \tag{12}$$

for $r < R$ and $V_C = Ze^2/r$ for $r > R$. A reasonable approximation is to use Eq. (12) for all r, which serves to keep our treatment analytic. Where this approximation is inaccurate, the proton density is small, and the influence on the total energy is negligible (cf., Eq. 28).

We will optimize the total nuclear energy subject to the constraints

$$A = \int n d^3 r, \qquad N - Z = \int \alpha d^3 r, \tag{13}$$

producing the chemical potentials μ and $\bar{\mu}$:

$$\frac{\delta}{\delta n}[\mathcal{H} - \mu n] = 0, \qquad \frac{\delta}{\delta \alpha}[\mathcal{H} - \bar{\mu}\alpha] = 0. \tag{14}$$

These lead to

$$2\frac{d}{dr}\left[\mathcal{Q}n'\right] - \frac{\partial \mathcal{Q}}{\partial n}\left(n'\right)^2 = \frac{\partial \mathcal{H}_B}{\partial n} - \mu,$$
$$0 = \frac{\partial(\mathcal{H}_B + n_p V_C/2)}{\partial \alpha} - \bar{\mu} = 2S_2\alpha/n - V_C/2 - \bar{\mu}, \tag{15}$$

implicitly assuming $V_C \propto n_p = (n - \alpha)/2$. The second equation tells us that

$$\alpha = \frac{n}{2S_2}\left(\bar{\mu} + \frac{V_C}{2}\right) \tag{16}$$

and, together with the second constraint in Eq. (13), that

$$\bar{\mu} = \frac{2S_v I}{H_0} + \frac{3}{4}\frac{Ze^2}{R}\left(1 - \frac{H_2}{3H_0}\right), \tag{17}$$

where $I = (N - Z)/A$ and we define the dimensionless integrals

$$H_i = \int \frac{n}{A} \frac{S_v}{S_2} \left(\frac{r}{R}\right)^i d^3r. \tag{18}$$

Solving for α, we find

$$\alpha = \frac{n}{S_2} \left[\frac{S_v I}{H_0} + \frac{Ze^2}{8R} \left(\frac{H_2}{H_0} - \frac{r^2}{R^2} \right) \right]. \tag{19}$$

Inclusion of the Coulomb potential results in an increase in asymmetry at the center of the nucleus: protons are pushed outwards by Coulomb repulsion.

To make further progress, we examine $n(r)$. We approximate the symmetric energy density of uniform matter as $\mathcal{H}_B(n, 0) \simeq -B + (K/18)(1-u)^2$, where $B \simeq -16\,\text{MeV}$ is the bulk binding energy at saturation, K is the incompressibility parameter, and $u = n/n_s$. We also assume $\mathcal{Q} = Q/n$. Again assuming that $V_c \propto n_p$, and in the limit that $\alpha \to 0$, one finds

$$\mu = -B, \qquad u = \left(1 + e^{x-y}\right)^{-1} \tag{20}$$

where $r = ax$, $a = \sqrt{18Q/K}$ and y is determined from the first constraint in Eq. (13):

$$A = \int n d^3r = 4\pi n_s a^3 F_2(y), \tag{21}$$

where the standard Fermi integral is

$$F_i(y) = \int_0^\infty \frac{x^i dx}{1 + e^{x-y}} \simeq \frac{y^{1+i}}{1+i} \left[1 + \frac{i(i+1)}{6} \left(\frac{\pi}{y}\right)^2 + \cdots \right]. \tag{22}$$

This converges rapidly as $y \simeq r_o A^{1/3}/a \simeq 13$ for ^{208}Pb, where $4\pi n_s r_o^3/3 = 1$.

The parameter $K \simeq 240\,\text{MeV}$ from experiment, and the value of Q follows from the observed value of the 90–10 surface thickness:

$$t_{90-10} = a \int_{0.1}^{0.9} (u')^{-1} du = 4a \ln 3 \simeq 2.3 \text{ fm}, \tag{23}$$

giving $a = 0.523$ fm and

$$Q = \frac{K}{18} \left(\frac{t_{90-10}}{4 \ln 3} \right)^2 \simeq 3.65\,\text{MeV fm}^2. \tag{24}$$

As a check, the liquid droplet surface tension parameter is the semi-infinite, symmetric matter, surface thermodynamic potential per unit area:

$$
\sigma_o = \int_{-\infty}^{\infty} [\mathcal{H} - \mu n]dz = 2Q \int_{-\infty}^{\infty} \left(\frac{n'^2}{n} \right) dz
$$

$$
= \frac{Qn_s}{a} \simeq (1.12) \text{ MeV fm}^{-2}, \tag{25}
$$

using $Z/A \simeq 1/2$. This gives $E_s = 4\pi r_o^2 \sigma_o \simeq 18.3\,\text{MeV}$ for the symmetric matter surface energy parameter in the liquid droplet model, which is very close to the accepted value [15]. This energy density functional fits the most important observed properties of the symmetric matter nuclear interface, its tension and thickness, as well as the observed nuclear incompressibility.

Although Lipparini and Stringari assumed $S_2(n) = S_v + (L/3)(u - 1)$, this simplification is not necessary for analicity. If $S_2(n)$ can be represented by the convergent series expansion $S_2(u) = S_v(\sum_i b_i u^i)^{-1}$ in the domain $0 < u < 1$, the integrals H_i can be expanded in Fermi integrals and also, therefore, in $1/y$:

$$
H_i = \frac{4\pi n_s}{A} \frac{a^{3+i}}{R^i} \left[F_{2+i}(y) - (2+i)\mathcal{T}F_{1+i}(y) + \cdots \right] \simeq \frac{3}{3+i} - \frac{3\mathcal{T}}{y}, \tag{26}
$$

keeping only the leading terms in $y \propto A^{1/3}$. In turn, $\mathcal{T}$ is given by the expansion

$$
\mathcal{T} = b_1 + 3b_2/2 + 11b_3/6 + 25b_4/12 + 137b_5/60 \cdots, \tag{27}
$$

and $\sum_i b_i = 1$.

4.2 Relation of hydrodynamical model to liquid droplet model

Now we can relate the hydrodynamical model to the liquid droplet model. The total symmetry and Coulomb energies are

$$
E_{sym} + E_C = \int S_2 \frac{\alpha^2}{n} d^3r + \frac{1}{2} \int n_p V_C d^3r
$$

$$
= AI^2 \frac{S_v}{H_0} + \frac{3Z^2 e^2}{5R} \left[1 + \frac{AI}{8Z} \left(1 - \frac{5H_2}{3H_0} \right) \right]. \tag{28}
$$

The first term, representing the symmetry energy in the absence of the Coulomb potential, has the identical form to that in the liquid droplet model (to leading order in $A^{1/3}$), which is $S_v A/(1 + S_s A^{-1/3}/S_v)$, provided we make the association with the surface symmetry parameter

$$
\frac{S_s}{S_v} = -\frac{3}{y}\mathcal{T} = -\frac{3a}{r_o}\mathcal{T}. \tag{29}
$$

This allows one to compute the surface symmetry parameter directly in terms of the nuclear force parameters.

If the Lipparini & Stringari ansatz for S_2 is used, the values $b_0 = 1 + p$ and $b_1 = -p$, where $p = L/(3S_v)$, are found by expanding around $u = 1$. In this case, $\mathcal{T} = -p$ and $S_s = aL/r_o$. In practice, this provides a poor fit to realistic calculations. However, keeping an additional term in the expansion

$$S_2(u) \simeq S_v + L(u-1)/3 + K_{\text{sym}}(u-1)^2/18 + \cdots, \tag{30}$$

and setting $K_{\text{sym}} = 6L - 18S_v$ so that $S_2(0) = 0$, provides a much improved result. In this case, we find

$$b_0 = 2 + p^2, \quad b_1 = -2 + p - 2p^2, \quad b_2 = 1 - p + p^2,$$
$$\mathcal{T} = -\left(1 + p + p^2\right)/2, \quad S_s/S_v = (3a/2r_o)\left(1 + p + p^2\right). \tag{31}$$

This provides a reasonable approximation to realistic calculations (see Ref. [12]). Irrespective of the form for S_2, the symmetry and Coulomb energies become

$$E_{sym} + E_C = \frac{AI^2 S_v^2}{S_v + S_s A^{-1/3}} + \frac{3Z^2 e^2}{5R}\left[1 - \frac{AI}{12Z}\frac{S_s}{S_v A^{1/3} + S_s}\right], \tag{32}$$

showing explicitly the reduction of Coulomb energy due to polarization effects.

The dipole static polarizability, α_D, hereafter referred to simply as the dipole polarizability, is found by performing the constrained variation [13]

$$\frac{\delta}{\delta\alpha}\left(\int \mathcal{H}d^3r - \epsilon \int z\alpha d^3r\right) = 0, \tag{33}$$

with ϵ a small parameter. Defining α_d as the function $\alpha(r)$ which solves Eq. (33), the dipole polarizability is

$$\alpha_D = \frac{1}{2\epsilon}\int z\alpha_d d^3r. \tag{34}$$

The solutions for α_d and the dipole polarizability are

$$\alpha_d = n\frac{\epsilon z + V_C}{2S_2}, \quad \alpha_D = \frac{H_2 A R^2}{12S_v} \simeq \frac{AR^2}{20S_v}\left(1 + \frac{5}{3}\frac{S_s}{S_v A^{1/3}}\right), \tag{35}$$

where $z^2 = r^2/3$ within the integral. Note that the contribution from V_C vanishes because of symmetry. α_D is also related to the m_{-1} sum rule by $\alpha_D = 4m_{-1}$; for ^{208}Pb, $m_{-1} \simeq 6.9\,\text{fm}^2\,\text{MeV}^{-1}$.

The mean-square radii are

$$r_{n,p}^2 = \frac{1}{2(N, Z)}\int (n \pm \alpha)r^2 d^3r = \frac{R^2}{1 \pm I}\left[\frac{3}{5} \pm I\frac{H_2}{H_0} \pm \frac{Ze^2}{8ARS_v}\left(\frac{H_2^2}{H_0} - H_4\right)\right], \tag{36}$$

where $I = (N - Z)/A$. To lowest order, the root mean square neutron-proton radius difference, i.e., the neutron skin thickness, is then

$$r_{np} = \frac{2r_o(1 - I^2)^{-1/2}}{3(1 + S_s A^{-1/3}/S_v)}\sqrt{\frac{3}{5}}\left[I\frac{S_s}{S_v} - \frac{3Ze^2}{140r_oS_v}\left(1 + \frac{10}{3}\frac{S_s}{S_v A^{1/3}}\right)\right]. \quad (37)$$

Once again, we can see the effect of including the Coulomb potential: it reduces the neutron skin thickness by pushing protons towards the surface.

There is significant competition between volume and surface contributions in the formulae for the symmetry energy, dipole polarizability and neutron skin thickness of nuclei. As the volume-to-surface ratio scales as $A^{1/3}$, which only has an effective range between 3 and 6 in heavy nuclei, no single experiment can hope to sort out the individual contributions and thereby determine S_v and S_s, or equivalently, S_v and L, uniquely. Each case will, however, result in a correlation between these parameters with a different slope dL/dS_v. It is straightforward to estimate these slopes from the hydrodynamical model:

$$\left(\frac{dL}{dS_v}\right)_{mass} \simeq \frac{L}{S_v} + \frac{2R}{a}\left(1 + \frac{S_s}{S_v A^{1/3}}\right)(1 + 2p)^{-1} \simeq 19$$

$$\left(\frac{dL}{dS_v}\right)_{dipole} \simeq \frac{L}{S_v} + \frac{2R}{a}\left(\frac{3}{5} + \frac{S_s}{S_v A^{1/3}}\right)(1 + 2p)^{-1} \simeq 14$$

$$\left(\frac{dL}{dS_v}\right)_{skin} \simeq \frac{L}{S_v} - \frac{2R}{a}\left(\frac{3}{10} + \frac{S_s}{S_v A^{1/3}}\right)(1 + 2p)^{-1} \simeq -6, \quad (38)$$

where we used $L/S_v \simeq 3/2$, $S_s A^{-1/3}/S_v \simeq 1/4$ and $R \simeq 6.7$ fm (*i.e.*, Pb^{208}). Since the slopes of these correlations are different, these experiments, taken collectively, offer the hope of constraining symmetry parameters tightly.

4.3 The experimental constraints

We first examine the correlation determined by nuclear mass measurements. First consider the liquid drop model, a simplification of the droplet model, in which the total nuclear energy is expressed as

$$E(Z, A) = A(-B + S_v I^2) + A^{2/3}(E_s - S_s I^2)r + \frac{3}{5}\frac{e^2 Z^2}{r_0 A^{1/3}} + E_{shell} + E_{pairing}, \quad (39)$$

where $E_s \simeq 19$ MeV is the symmetric matter surface energy parameter. We will ignore shell and pairing effects for the present discussion. The net symmetry energy of an isolated nucleus is then

$$E_{DM,i} = I_i^2(S_v A_i - S_s A_i^{2/3}). \quad (40)$$

The parameters are typically determined by a least-squares fit to measured masses, i.e., minimizing the differences between model predictions and experimentally measured symmetry energies,

$$\chi^2 = \sum_i (E_{\exp,i} - E_{\mathrm{DM},i})^2/\sigma_{\mathrm{DM}}^2, \qquad \bar{\chi}^2 \equiv \chi^2/\mathcal{N} \qquad (41)$$

where $\mathcal{N}$ is the total number of nuclei and σ_{DM} is a nominal error. A $\bar{\chi}^2$ contour one unit above the minimum value represents the 1σ confidence interval which is an ellipse in this linear example.

The properties of the confidence ellipse are determined by the second derivatives of $\bar{\chi}^2$ at the minimum,

$$[\bar{\chi}_{vv}, \bar{\chi}_{vs}, \bar{\chi}_{ss}]\sigma_{\mathrm{DM}}^2 = 2\mathcal{N}^{-1} \sum_i I_i^4 [A_i^2, -A_i^{5/3}, A_i^{4/3}] \simeq 61.6, -10.7, 1.87, \qquad (42)$$

where $\bar{\chi}_{vs} = \partial^2 \bar{\chi}^2/\partial S_v \partial S_s$, etc. The specific values quoted follow from the set of 2336 nuclei with N and Z greater than 40 from Ref. [16]. The confidence ellipse in $S_s - S_v$ space has orientation $\alpha_{\mathrm{DM}} = (1/2) \tan^{-1} |2\bar{\chi}_{vs}/(\bar{\chi}_{vv} - \bar{\chi}_{ss})| \simeq 9.8°$ with respect to the S_s axis, with error widths $\sigma_{v,\mathrm{DM}} = \sqrt{(\bar{\chi}^{-1})_{vv}} \simeq 2.3\sigma_{\mathrm{DM}}$ and $\sigma_{s,\mathrm{DM}} = \sqrt{(\bar{\chi}^{-1})_{ss}} \simeq 13.2\sigma_{\mathrm{DM}}$ where $(\bar{\chi}^{-1})$ is the matrix inverse. The correlation coefficient is $r_{\mathrm{DM}} = \bar{\chi}_{vs}/\sqrt{\bar{\chi}_{vv}\bar{\chi}_{ss}} \simeq 0.997$.

In this example, the shape and orientation of the confidence interval depend only on A_i and I_i and not on the binding energies themselves or the location of the $\bar{\chi}^2$ minimum or the other drop parameters. This correlation is therefore largely model-independent and the most valuable of constraints from nuclear experiment. It is straightforward to see that the droplet model energy, Eq. (32), will give a very similar correlation. In this case, however, there will be a small dependence of the second derivatives χ on the position of the minimum as well as the measured energies, in contrast to the liquid drop case.

We now proceed to examine correlations between L and S_v that have been experimentally determined. This summary is largely taken from Lattimer and Lim [12]. The correlation between L and S_v for measured nuclear masses is taken from Hartree-Fock calculations with the UNEDF0 density functional [19], in which the nominal fitting error was arbitrarily chosen to be $\sigma = 2\,\mathrm{MeV}$. In all likelihood, this value is overestimated, as negative values for L, which give negative neutron matter pressures, are reached. Instead, we choose $\sigma = 1\,\mathrm{MeV}$. Importantly, the shape and orientation of the ellipse are rather steep in both $S_s - S_v$ (as already seen for the liquid drop model) and $L - S_v$ space. It agrees with the hydrodynamical model prediction.

The constraints for the neutron skin thickness of ^{208}Pb are taken from a study by Chen et al. [20], who converted the experimental results for Sn isotopes into an equivalent value for ^{208}Pb: $r_{np} \simeq (0.175 \pm 0.020)$ fm. They also established, from a study of Skyrme Hartree-Fock calculations of ^{208}Pb in which S_v and L were systematically varied,

Fig. 6 Experimental constraints
for symmetry energy
parameters, adapted and revised
from [12]. See the text for
further discussion. G and H refer
to the neutron matter studies of
Gandolfi et al. [17] and Hebeler
et al. [18], respectively
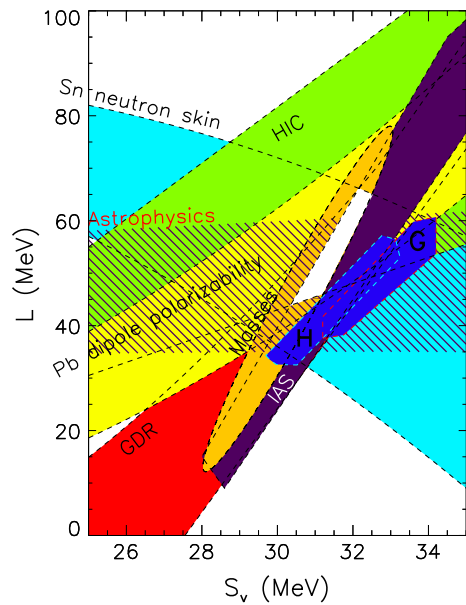
$$\frac{r_{np}}{\text{fm}} \simeq -0.094669 + \frac{7.2028 S_v}{\text{GeV}} + \frac{2.3107 L}{\text{GeV}}$$
$$- \frac{8.8453 S_v^2}{\text{GeV}^2} - \frac{47.837 S_v L}{\text{GeV}^2} + \frac{4.003 L^2}{\text{GeV}^2}. \tag{43}$$

This formula, with the aforementioned value for r_{np}, establishes the correlation slope
$d \ln L / d \ln S_v \simeq -3.75$, assuming $S_v = 31 \, \text{MeV}$ and $L = 45 \, \text{MeV}$. This is less
steep than predicted by the hydrodynamical model (-6), and should be explored with
a greater variety of effective interactions.

Similarly, the constraint for the electric dipole polarizability α_D of ^{208}Pb is taken
from data produced by Tamii et al. [21]: $\alpha_D \simeq (20.1 \pm 0.6) \, \text{fm}^3$. Roca-Maza et al. [22]
showed, from studies with a series of relativistic and non-relativistic interactions, that
the dipole polarizability, bulk symmetry parameter, and the neutron skin thickness for
^{208}Pb can be constrained by

$$\alpha_D S_v \simeq (325 \pm 14) + (1799 \pm 70)(r_{np}/\text{fm}) \, \text{Mev fm}^3. \tag{44}$$

Equation (43) convert this onto the $S_v - L$ correlation shown in Fig. 6.

Equation (44) is not the same as that from the hydrodynamical model. Although
the predicted slopes of both correlations are positive and somewhat less steep than that
of nuclear masses, the functional difference suggests that the correlation of Ref. [22]
might be model-dependent and should be further explored. The slope of this correlation
is significantly different than shown in Ref. [12], which relied on the erroneous result
$\alpha_D \propto r_{np}$ derived in Ref. [23].

The constraint for the centroid energy of the giant dipole resonance for ^{208}Pb is taken from Ref. [24] who concluded that the measured energy was best fit by those forces having a bulk symmetry energy, evaluated at the density $n = 0.1\,\mathrm{fm}^{-3}$, in the range $S_2(0.1) \simeq (24.1 \pm 0.9)\,\mathrm{MeV}$. Lattimer and Lim [12] deduced the band shown in Fig. 6 by studying a wide range of plausible density functionals. Unfortunately, the hydrodynamical model does not yield an analytic prescription for this correlation, but one should expect it to be similar to that of the dipole polarizability, borne out as shown in Fig. 6.

Additional correlations depicted in Fig. 6 are due to isospin diffusion in heavy-ion collisions [25] and excitation energies to isobaric analog states by Danielewicz & Lee [26]. The model-dependence of isotope diffusion studies has not been explored, although the depicted results are consistent with multifragmentation studies in intermediate-energy heavy ion collisions [27] which imply $40\,\mathrm{MeV} < L < 125\,\mathrm{MeV}$. And while excitation energies are sensitive to shell effects, they are closely related to ground state energies. Thus, the latter correlation bears a great deal of resemblance to that determined from nuclear binding energies. Danielewicz & Lee also combined their analysis with measurements of the ^{208}Pb skin thickness to further restrict the allowed $S_v - L$ parameter space. Using a weighted average $r_{np} = (0.179 \pm 0.023)\,\mathrm{fm}$, a slight 0.004 fm larger than in Ref. [20] and used in Fig. 6, they found $33\,\mathrm{MeV} < L < 72\,\mathrm{MeV}$ (not shown in Fig. 6).

In contrast, the white region in Fig. 6 represents the consensus agreement of the five experimental constraints we have discussed, giving a somewhat smaller range $44\,\mathrm{MeV} < L < 66\,\mathrm{MeV}$. (The consensus region displayed in Fig. 6 is slightly smaller than in Ref. [12] because of the additional constraint from isobaric analog states.) Since the model dependencies of these constraints have not been thoroughly explored, the size of this consensus region may well be underestimated. If we treat the white region as a 68 % confidence interval for the experimental determination of S_v and L, it can be used with Monte Carlo sampling to determine a distribution of neutron star matter pressures at n_s by means of Eq. (10). Then, using Eq. (5), the 90 % CI for radii of $1.4M_\odot$ stars is found to be $R_{1.4} \simeq (12.1 \pm 1.1)\,\mathrm{km}$. As we will see, this range is quite compatible with several astrophysical observations.

4.4 Neutron matter studies

Two recent studies of pure neutron matter using realistic two- and three-nucleon interactions coupled with low-energy scattering phase shift data, the first employing chiral Lagrangian methods [18] and the second using quantum Monte Carlo techniques [17], can also render constraints on symmetry energy coefficients and neutron star radii [28,29]. With the important assumption that higher-than-quadratic terms in Eq. (6) are ignored, the values of the neutron matter energy and pressure at n_s provide direct estimates of S_v and L. The estimated error ranges for the symmetry parameters determined [18] from neutron matter studies are also displayed in Fig. 6. These estimates are very consistent with those determined from nuclear experiments. The small displacement of the neutron matter results may represent the effects of neglecting quartic or higher-order terms in the symmetry energy expansion.

5 Estimates of neutron star radii

Although nearly three dozen neutron star masses have been determined very accurately [1], there are no precise simultaneous measurements of any star's mass and radius (accuracies typically are less than 20 %). To date, several different astrophysical measurements of neutron star radii have been attempted. We will focus attention on radius estimates inferred from photospheric radius expansion bursts and thermal emissions from quiescent low-mass X-ray binaries and isolated neutron stars. A 20 % uncertainty in the measurement of R translates into nearly a 100 % uncertainty for the determination of L, since $L \propto R^4$ using Eqs. (10) and (5), which is substantially larger than the accuracy afforded by nuclear experiments and neutron matter theory[12]. Moreover, with such large errors in M and R for individual sources, direct inversion of the TOV structure equations cannot credibly limit the pressure-density relation.

Even taking the ensemble of measurements and attempting to invert the structure equations to infer the $M - R$ relation is problematic without physical guidance. How does one choose the weighting for a particular EOS and $M - R$ curve: does one place more emphasis on its passing close to the central values of the measurements, or does one integrate the effective weight along the entire $M - R$ curve? Fortunately, Bayesian techniques exist to alleviate this problem. The body of observations can be coupled to the structure equations, as shown by Ref. [30], to effectively determine the $M - R$ relation and, further, to obtain estimates of the pressure-density relation of neutron star matter, not only near ρ_s, but up to the highest densities found in neutron star interiors. The deduced uncertainty of the pressure of high-density matter can be as large as 150 % but is generally much smaller.

5.1 Photospheric radius expansion bursts

X-ray bursts on neutron star surfaces often occur from the unstable burning of material accreted companions in X-ray binaries. The nuclear burning spreads across the stellar surface and gives rise to a sudden increase in X-ray luminosity and temperature. Some of these X-ray bursts are energetic enough to reach the so-called Eddington limit at which radiation pressure is sufficiently large to overcome gravity, leading to expansion of the star's photosphere. These photospheric radius expansion (PRE) bursts can constrain M and R because the largest observed flux during the burst must be near the Eddington limit

$$F_{\text{Edd},\infty} = \frac{cGM}{\kappa D^2} \sqrt{1 - \beta_{ph}} \qquad (45)$$

where $\beta_{ph} = 2GM/R_{ph}c^2$ and R_{ph} is the effective radius of the photosphere when this flux is measured. Özel and collaborators [31–35] have studied 5 burst sources. While they assumed that $R_{ph} = R$, Steiner et al. [30] argued that R_{ph} is larger, making the redshift negligible. In any case, measurement of the peak flux constitutes an observable which is a function of M, κ, D, and possibly R. The reproducibility of the maximum

flux from repeated bursts from the same source supports the identification of this flux with the Eddington limit.

A second observable in these systems is the nearly constant angular emitting area inferred several seconds after the burst's peak. The emission seems nearly thermal, and simultaneous measurement of the observed flux and temperature can yield an angular diameter (which is redshifted) if the correction $f_c = T_c/T_{eff}$ between effective temperature and color temperature, which represents the effects of an atmosphere, is known:

$$A \equiv \frac{F_\infty}{\sigma T_{eff,\infty}^4} = f_c^{-4} \left(\frac{R_\infty}{D}\right)^2, \qquad (46)$$

where $R_\infty = R/\sqrt{1 - 2\beta}$ is the apparent radiation radius and $T_{eff,\infty} = T\sqrt{1 - 2\beta}$ is the observed effective temperature. Repeated bursts from the same source show the same emitting areas, suggesting strongly that the entire neutron star surface is emitting during the cooling tail and that non-spherically symmetric effects during this phase are small. The observable A is thus a function of M, R, f_c and D. With knowledge of D, f_c and κ, the mass and radius can be deduced from $F_{Edd,\infty}$ and A. The opacity in these high-temperature sources is dominated by electron scattering, $\kappa = 0.200 m_B^{-1}(1 + X) \, \text{cm}^2 \, \text{g}^{-1}$, where m_B is the baryon mass and $0 < X < 0.7$ is the H mass fraction. This range for X reflects uncertainty in the composition: He at one extreme and solar at the other. Also, we assume that $f_c = 1.40 \pm 0.07$, a slightly larger range than Özel et al. assumed. The uncertainty distributions for κ and f_c are taken to be boxcar shaped.

In the extreme case that $z_{ph} = 0$, we can form two variables

$$\alpha = \frac{F_{Edd,\infty}}{\sqrt{A}} \frac{\kappa D}{f_c^2 c^3} = \beta\sqrt{1 - 2\beta}, \qquad \gamma = \frac{A}{F_{Edd,\infty}} \frac{f_c^4 c^3}{\kappa} = \frac{R}{\beta(1 - 2\beta)}, \qquad (47)$$

from which M and R are found:

$$\beta = \left[1 + \sqrt{3}\sin(\theta/3) - \cos(\theta/3)\right]/6,$$
$$R = \alpha\gamma\sqrt{1 - 2\beta}, \qquad M = \alpha^2\gamma c^2/G, \qquad (48)$$

where $\theta = \cos^{-1}(1 - 54\alpha^2)$. When $\alpha < 3^{-3/2} \simeq 0.192$, θ is real and there are 3 real roots for β. One of these is negative, and another is greater than 1/3 which nearly violates the causality constraint for neutron stars. The remaining real root is the one given in Eq. (48). When $\alpha > 3^{-3/2}$, θ and all roots for β are imaginary. All five sources have $\alpha < 0.192$. Ref. [30] noted when $R_{ph} = R$, the reality condition is $\alpha < 1/8$ which is not observed for any source. Monte Carlo sampling of the observables $F_{Edd,\infty}$, A and D and the parameters X and f_c within their uncertainty ranges yields the $M - R$ probability distributions shown in Fig. 7. The average mass and radius implied by these results are $\bar{R} = 10.77 \pm 0.65 \, \text{km}$ and $\bar{M} = 1.65 \pm 0.12 M_\odot$. As neutron star radii don't change much with M, the relatively small standard deviation in R is interesting.
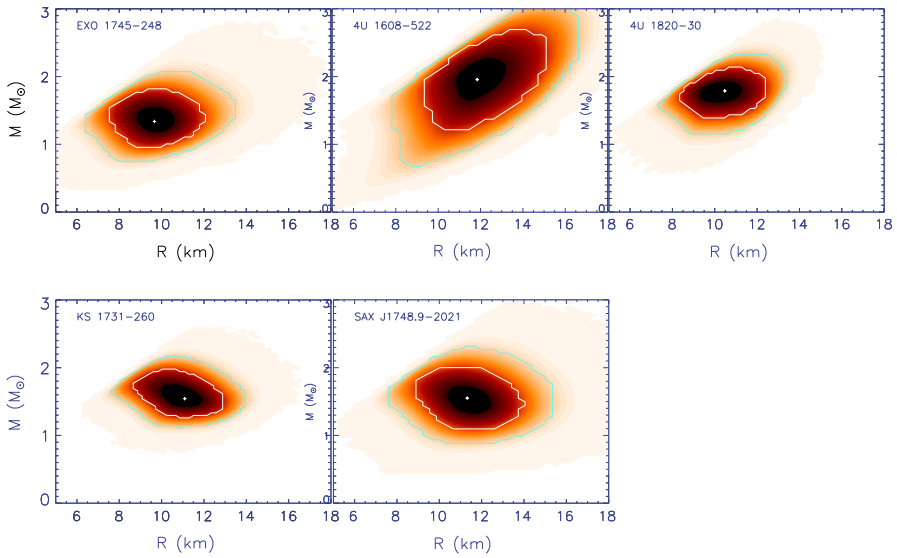
Fig. 7 $M - R$ probability contours for PRE X-ray burst sources (data from Refs. assuming $R_{ph} \gg R$. *Crosses* indicate maximum probabilities and *white (blue) contours* are 1σ (2σ) (color figure online)

5.2 Quiescent low-mass X-ray binaries

Certain neutron stars in binary systems may intermittently accrete matter from an evolving companion star, with episodes of accretion separated by long periods of quiescence. While the neutron star accretes, compression of matter in the crust induces nuclear reactions that release heat in sufficient amounts to warm the star to temperatures not seen since its birth. These stars then cool via neutrino radiation from their interiors and X-rays from their surfaces. It is generally believed that accretion suppresses surface magnetic fields, which is an advantage of using these systems for radius measurements compared to isolated neutron stars for which strong, uncertain, magnetic fields may exist. Strong magnetic fields can significantly affect a star's atmosphere and introduce large uncertainties in radius measurements. In addition, due to the rapid gravitational settling timescales (of order seconds), only the lightest element in accreted matter remains in its atmosphere. Thus, these transient X-ray sources, also known as quiescent low-mass X-ray binaries (QLMXBs) are believed to have low-magnetic field H or He atmospheres. The emitted X-ray spectra, for a given composition, will depend largely on R and T_{eff}, and, to a lesser extent, on the gravity $g = GM(1+z)/R^2$.

In contrast, the observed spectrum will depend on the distance D and on the amount of interstellar absorption between the source and the observer, usually parameterized by N_H, the column density of H. The absorption is important, as it has an energy dependence of $E^{-8/3}$ and can significantly reduce the observed flux near the peak and at lower energies. It is often difficult to determine distances to field sources while distance determinations of globular clusters are relatively
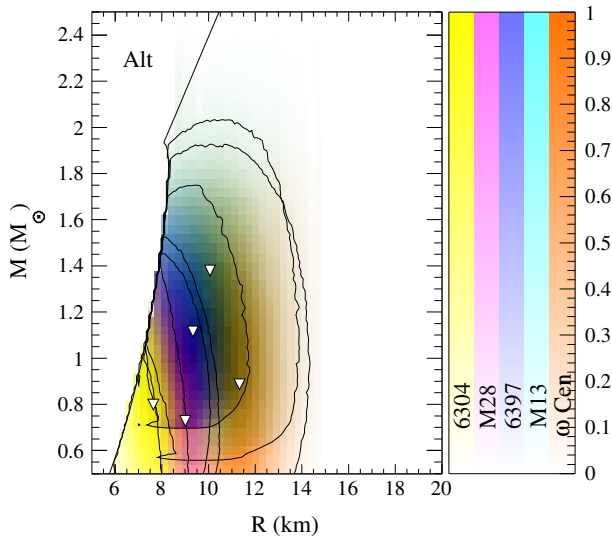
Fig. 8 Probability distributions in M and R for the 5 QLMXBs studied by Guillot et al. [36], revised to reflect fixed N_H values from Ref. [37] using the procedure described in Ref. [14]. *Color coding* for the relative probabilities are indicated by the *bar graphs* on the *right*, which are ordered according to their most probable radii (marked by *triangles*). *Solid curves* denote 90 % confidence boundaries. The *left-most curve* bounds the region permitted by causality and the $\hat{M} = 2M_\odot$ constraints. Figure taken from Ref. [14]

accurate. For this reason, attention has been focused on systems in globular clusters.

Fitting the observed spectrum provides estimates for R_∞, $T_{\mathrm{eff},\infty}$, g and N_H, but due to lack of resolution and poor statistics, the deduced N_H [36] is often at odds with the amount of absorption deduced from HI radio surveys [37]. An underestimate of absorption will lead to an underestimate of mass and radius, because it has a similar effect to underestimating the distance.

Guillot et al. [36] recently summarized the observed properties of 5 QLMXBs with known distances and modeled them with H atmospheres to derive masses, radii and H column densities. The most striking feature in their results is that the optimum inferred values of R_∞ range from 8.4 to 23.0 km, of R from 6.4 to 19.4 km, and of M from 1.25 to 2.69 $M_\odot$. Such large variations are not expected from evolutionary considerations for a relatively uniform class of sources. Lattimer and Steiner [14] argued that the most extreme values of R_∞ were associated with the largest discrepancies between inferred values of N_H and those independently determined from radio observations. Using an analytic approximation to model the effects of variations in N_H, Ref. [14] estimated new values of R_∞ using the alternate N_H values from Ref. [37] for each source. The revised estimates for the inferred $M - R$ distributions for the 5 sources are shown in Fig. 8, after removing regions that violate causality and the $\hat{M} = 2M_\odot$ constraint. In this analysis, inferred values for z were barely affected. Values of R_∞, R and M now have much smaller variances and range from 9.4 to 13.2 km, 7.8 to 11 km, and 1.23 to 1.64 $M_\odot$.

6 Bayesian analysis of mass and radius observations

The basic problem we want to solve is how to compute the M-R curve from a set of neutron star mass and radius observations. We also want to compute the EOS, taking advantage of the well-known bijection between the M-R curves and EOSs provided by the TOV equations. The first critical point is that observations are never perfectly accurate, and thus this problem has an inherently statistical nature: what we really want is the probability distribution of M-R curves and EOSs. The second critical point is that this is a highly underconstrained problem: a curve has an infinite number of degrees of freedom, and we will always have only a finite set of observations. Bayesian statistics is thus already a natural choice, since its application to underconstrained problems is a bit simpler. In an overconstrained least-squares problem, there can be one unique best fit represented by a point in the model space. In the underconstrained system, there is no unique best-fit, but rather an entire subspace inside our model space which consists of "best-fits". As we will see below, Bayes theorem provides for us a recipe for characterizing that subspace.

The joint probability of event a in event space A and event b in event space B can be denoted $P[A, B]$, normalized by $1 = \int_A \int_B P[A, B]\, da\, db$. The marginal probability $P[A]$ is then given by $P[A] = \int_B P[A, B]\, db$ and similarly for $P[B]$. The conditional probability is then defined by $P[A|B] \equiv P[A, B]/P[B]$, i.e. the probability of A given B. From this definition, the celebrated Bayes theorem can be be written $P[A|B]P[B] = P[B|A]P[A]$. In our context, we replace A with the model space $\mathcal{M}$ and B with the data space $\mathcal{D}$.

By analogy to the definitions above,

$$P[\mathcal{D}] = \int_{\mathcal{M}} P[\mathcal{D}, \mathcal{M}]\, dm = \int_{\mathcal{M}} P[\mathcal{D}|\mathcal{M}]P[\mathcal{M}]\, dm \tag{49}$$

(this is sometimes referred to as the "law of total probability") and thus

$$P[\mathcal{M}|\mathcal{D}] = \frac{P[\mathcal{D}|\mathcal{M}]P[\mathcal{M}]}{\int_{\mathcal{M}} P[\mathcal{D}|\mathcal{M} = m]P[\mathcal{M}]\, dm} \tag{50}$$

What we want to compute is the conditional probability of all models in our model space, given the data d actually observed inside the space of all possible data sets $\mathcal{D}$, i.e. $P[\mathcal{M}|\mathcal{D} = d]$. In some cases we only require relative probabilities, i.e. $P[\mathcal{M} = m_1|\mathcal{D} = d]/P[\mathcal{M} = m_2|\mathcal{D} = d]$ for models m_1 and m_2 inside our model space $\mathcal{M}$, so the integral in the denominator is unimportant. The function $P[\mathcal{D}|\mathcal{M}]$ is analogous to the likelihood function familiar from frequentist statistics, and $P[\mathcal{M}]$ is referred to as the prior distribution, reflecting the prior probability of a given model m.

In a typical data set of several one-dimensional data points, the likelihood function is just a multi-dimensional Gaussian. Our neutron star data set is inherently two-dimensional. A typical frequentist approach is to minimize the distance from the the observed data point (R, M) and the model $M - R$ curve. (This is ambiguous because one must still choose the relevant mass and radius scales to measure a distance.) One

way to proceed in the Bayesian formalism is to treat the mass of each neutron star as a new model parameter. Our model space, $\mathcal{M}$, now includes the neutron star masses, M_i in addition to the EOS parameters p_i. If the observations were two-dimensional Gaussians centered at $(R_{\text{obs},i}, M_{\text{obs},i})$ with widths $(\sigma_{R,i}, \sigma_{M,i})$, the conditional probability would be

$$P[\mathcal{D}|\mathcal{M}] = \prod_{i=1}^{N_O} \left(2\pi\sigma_{M,i}\sigma_{R,i}\right)^{-1}$$

$$\times \exp\left[-\frac{1}{2}\left(\frac{M_i - M_{\text{obs},i}}{\sigma_{M,i}}\right)^2 - \frac{1}{2}\left(\frac{R_i(M_i, \{p_j\}) - R_{\text{obs},i}}{\sigma_{R,i}}\right)^2\right] \quad (51)$$

for N_O neutron star observations. The function $R_i(M_i, \{p_j\})$ requires a solution of the TOV equations for each point in the model space. In general, the observations are not two-dimensional Gaussians, so the conditional probability for each observation is a general distribution $\mathcal{D}_i(R_i, M_i)$ normalized so that $\int dR_i\, dM_i\, \mathcal{D}_i(R_i, M_i) = 1$.

The full prior probability, $P[\mathcal{M}]$, in this context is now an $(N_P + N_O)$-dimensional function reflecting the prior probability given a set of N_P EOS parameters and N_O neutron star masses. It is reasonable to assume that the prior can be factorized into separate prior distributions for the EOS and the masses, and that they are both uniform.

Bayes theorem itself is a basic result which can be obtained from basic axioms of probability theory. The frequentist and Bayesian approaches diverge in how the theorem ought to be applied. The standard Bayesian approach is to compute the desired results by integrating (marginalizing) over the parameters not currently being considered. Explicitly, for the posterior probability distribution of one of the EOS parameters, p_i, one computes the integral

$$P[p_i] = \int P[\mathcal{D}|\mathcal{M}]P[\mathcal{M}]dp_1 \ \ldots \ dp_{i-1}dp_{i+1} \ \ldots \ dp_{N_p}dM_1 \ \ldots \ dM_{N_O}. \quad (52)$$

One can compute the 68 % confidence region, which for a unimodal posterior, is the range (p_{iL}, p_{iR}) surrounding the maximum value of $P[p_i]$ for which $P[p_{iL}] = P[p_{iR}]$ and

$$0.68 = \int_{p_{iL}}^{p_{iR}} P[p_i]\, dp_i \Big/ \int P[p_i]\, dp_i. \quad (53)$$

6.1 Results of Bayesian analysis

We employ the model of Ref. [30], using a neutron star crust, a phenomenological EOS near the saturation density, and the implicit assumption that the TOV equations relate the EOS to M and R. At high densities, we use two polytropes, ensure causality and $\hat{M} \geq 2M_\odot$. For QLMXBs, we use values of N_H from Ref. [37] and allow for either H or He atmospheres (except for the source in ω Cen). We assume $R_{ph} >> R$
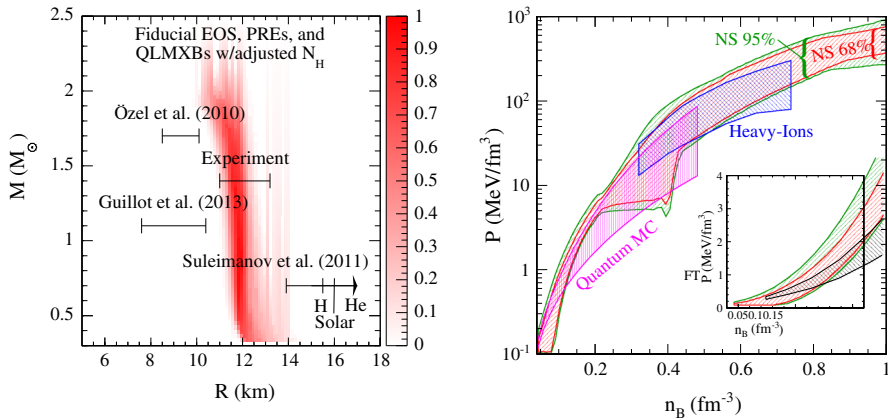
Fig. 9 *Left panel*: Bayesian probability distributions for M and R for the five PRE burst sources, assuming $z_{ph} = 0$, and five QLMXB sources, assuming values of N_H from Ref. [37] and the possibility of either H or He atmospheres for four of the sources. Radius ranges of Ozel et al. (95 % confidence [31–35]), Guillot et al. (joint analysis assuming a common radius for all masses [36]), Suleimanov et al. (90 % CI for pure H, solar with $Z = 0.02$, and pure He atmospheres [39]), and nuclear experiments (90 % CI for $1.4M_\odot$ stars, [12]) are shown for comparison (arbitrary *vertical* locations). Figure taken from Ref. [14]. Right panel: The inferred EOS, whichs is parametrized with two polytropes at high density. Figure taken from Ref. [38]

for the PRE sources. The predicted $M - R$ distribution for the ensemble of 5 PRE and 5 QLMXB sources is shown in Fig. 9 and observed to be relatively vertical. The range of radii for a $1.4M_\odot$ neutron star, 11.3–12.1 km (68 % confidence) is slightly larger than that given in Ref. [38], a consequence of the larger radii implied by the possibility of He atmospheres in four of the QLMXB sources. This figure also shows the inferred EOS from Ref. [38] which is similar to the present case.

How sensitive are our results are to the nature of the astronomical sources? The 90 % CI for the radii of $1.4M_\odot$ stars is increased by 0.3–0.4 km if only PRE burst sources are considered, while the radii are increased by 0.1–0.2 km if only QLMXB sources are included. These small differentials imply that our results are not very sensitive to the type of source included, and that the constraints of maximum mass, causality, a hadronic crust EOS and the TOV equation are powerful. The lower limit on the radius from QLMXB sources is 11.2 km, and adding the PRE sources (which have significant probability at low radius) implies only a slightly smaller lower limit of 11.1 km.

Our results bear significant differences from those of Özel et al, Guillot et al., and Suleimanov et al. [39], as shown in Fig. 9. We attribute this, in varying degrees, not only to different prior assumptions but also to the neglect of a neutron star crust, causality and $\hat{M} = 2M_\odot$ in these analyses.

To compare two models, $\mathcal{M}_1$ and $\mathcal{M}_2$, one uses the Bayes factor

$$B_{12} = \frac{\int_{\mathcal{M}_1} P[\mathcal{D}|\mathcal{M}_1 = m_1] P[\mathcal{M}_1 = m_1]\, dm_1}{\int_{\mathcal{M}_2} P[\mathcal{D}|\mathcal{M}_2 = m_2] P[\mathcal{M}_2 = m_2]\, dm_2} \tag{54}$$

If $B_{12} > 1$, then model 1 is preferred, and if $B_{12} < 1$, then model 2 is preferred. A typical phrasing is that $B_{12} > 3$ implies the evidence for model 1 is substantial,

$B_{12} > 10$ implies the evidence is strong, $B_{12} > 30$ implies the evidence is very strong, $B_{12} > 100$ implies the evidence is decisive. The Bayes factor provides decisive support for our assumptions that $R_{ph} >> R$ in PRE sources and, in QLMXBs, for independently determined values of N_H, as well as the possibility that some of the sources have He, rather than, H atmospheres.

The neutron star observations constrain the nuclear symmetry energy through the correlation Eq. 5, yielding a 68 % confidence range on L between 37.0 and 55.3 MeV (Fig. 6). This range is similar to that found in Ref. [38] except the lower range for L has been decreased because of the very small radii of the neutron stars in globular clusters NGC 6304 and M28. Using a different EOS parameterization which allows for stronger phase transitions increases the upper 68 % confidence limit on L to about 65 MeV. This happens because a phase transition partially decouples the low- and high-density behavior of the EOS, allowing small radii even if L is relatively large.

7 Conclusions

A plethora of nuclear experimental data argue that the symmetry energy parameters S_v and L are constrained to a greater degree than just a few years ago. Although these constraints have varying degrees of model dependence which need to be further explored, they are well-supported by studies of pure neutron matter if higher-than-quadratic terms in the symmetry energy expansion in neutron excess are ignored.

In comparison, the astrophysical determination of individual neutron star radii have much less confidence. Nevertheless, Bayesian studies (cf., [30,38]) of the ensemble of sources for which both mass and radius information is available imply radii for $1.2 - 1.8 M_\odot$ stars lie in the range 11.2–12.8 km. There is thus emerging an important concordance between the astronomical observations and the nuclear experiments. With almost any reasonable assumptions regarding the nature of the EOS at high densities and the parameters of models for shorter PRE X-ray bursts and QLMXBs, the powerful constraints of causality, observation of $2M_\odot$ neutron stars, and the existence of a nuclear neutron star crust, lead to $M - R$ curves which are nearly vertical and radii for moderate-mass neutron stars that are compatible with nuclear data and theoretical studies of neutron matter.

In the future, additional methods of measuring neutron star masses and radii will be possible. The NICER [40] and LOFT [41] space observatories will allow X-ray timing and spectroscopy of thermal and non-thermal emissions. Hot or cold regions on rotating neutron stars alter the shapes of X-ray pulses, and theoretical modeling of observed pulse profiles should allow measurements of surface redshifts. In addition, phase-resolved spectroscopy has the potential of directly measuring R. Recent analyses [42] of pulse profiles using existing instruments give overall results that are consistent with the $M - R$ curve illustrated in Fig. 9, but have very large uncertainties. The moment of inertia of a neutron star depends primarily on MR^2, and might be measurable in close binary systems where spin-orbit coupling is observed, such as PSR 0737-3039 [43]. In this system, ten-years worth of additional observations might determine the moment of inertia of pulsar A to about 10 % accuracy [44], which would determine the radius to about 5 %. Another method of obtaining moment of inertia information

is from estimates of the fraction of the moment of inertia contained in the neutron star crust as deduced from pulsar glitches. The standard model for pulsar glitches holds that they are due to the neutron superfluid in the star's crust. A pulsar with a regular history of glitches, Vela, suggests a crustal fraction of at least 1.6% [45] which is consistent with the fraction of about 4% stemming from the values of L we find [12]. We could also mention that supernova neutrinos, quasi-periodic oscillations from accreting sources (which could measure the innermost stable circular orbit radius), and gravitation waves (which could measure dipole and quadrupole polarizabilities, and the onset of tidal disruption of the neutron star) from compact binary mergers, also offer potential methods of measuring neutron star radii. The latter topic is discussed further in other contributions to this volume.

References

1. Lattimer, J.M.: Annu. Rev. Nucl. Part. Sci. **62**, 485 (2012)
2. Page, D., Prakash, M., Lattimer, J.M., Steiner, A.W.: Phys. Rev. Lett. **106**, 081101 (2011)
3. Shternin, P.S., et al.: MNRAS **412**, 108 (2011)
4. Demorest, P.B., et al.: Nature **467**, 1081 (2010)
5. Antoniadis, J., et al.: Science **340**, 448 (2013)
6. Koranda, S., Stergioulas, N., Friedman, J.L.: ApJ **488**, 799 (1997)
7. Rhoades Jr, C.E., Ruffini, R.: Phys. Rev. Lett. **32**, 324 (1974)
8. Glendenning, N.K.: Phys. Rev. **D46**, 4161 (1992)
9. Lattimer, J.M., Prakash, M.: ApJ **550**, 426 (2001)
10. Lattimer, J.M., Prakash, M.: Phys. Rev. Lett. **94**, 111101 (2005)
11. Lattimer, J.M., Prakash, M.: In: Lee S. (ed.) From Nuclei to Stars. (World Scientific, Hong Kong), p. 275 (2010), arXiv:1012.3208
12. Lattimer, J.M., Lim, Y.: ApJ **771**, 51 (2013)
13. Lipparani, E., Stringari, S.: Phys. Rep. **103**, L175 (1989)
14. Lattimer, J.M., Steiner, A.W.: EPJA **50**, 40 (2014). arXiv:1305.3242
15. Myers, W.D., Swiatecki, W.J.: Ann. Phys. **55**, 395 (1969)
16. Audi, G., Wapstra, A.H., Thibault, C.: Nucl. Phys. A **729**, 337 (2003)
17. Gandolfi, S., Carlson, J., Reddy, S.: Phys. Rev. C **85**, 032801 (2012)
18. Hebeler, K., Lattimer, J.M., Pethick, C.J., Schwenk, A.: Phys. Rev. Lett. **105**, 161102 (2010)
19. Kortelainen, M., et al.: Phys. Rev. C **82**, 024313 (2010)
20. Chen, L.-W., Ko, C.M., Li, B.-A., Xu, J.: Phys. Rev. C **82**, 024321 (2010)
21. Tamii, A., et al.: Phys. Rev. Lett. **107**, 062502 (2011)
22. Roca-Maza, X., et al.: Phys. Rev. C **88**, 4316 (2013)
23. Reinhard, P.-G., Nazarewicz, W.: Phys. Rev. C **81**, 051303 (2010)
24. Trippa, L., Coló, G., Vigezzi, E.: Phys. Rev. C **77**, 061304 (2008)
25. Tsang, M.B., et al.: Phys. Rev. Lett. **102**, 122701 (2009)
26. Danielewicz, P., Lee, J.: Nucl. Phys. A **922**, 1 (2014). arXiv:1307.4130
27. Shetty, D.V., Yennello, S.J., Souliotis, G.A.: Phys. Rev. **C76**, 024606 (2007)
28. Steiner, A.W., Gandolfi, S.: Phys. Rev. Lett. **108**, 081102 (2012)
29. Hebeler, K., Lattimer, J.M., Pethick, C.J., Schwenk, A.: ApJ **773**, 11 (2013)
30. Steiner, A.W., Lattimer, J.M., Brown, E.F.: ApJ **722**, 33 (2010)
31. Özel, F., Güver, T., Psaltis, D.: ApJ **693**, 1775 (2009)
32. Güver, T., Özel, F., Cabrera-Lavers, A., Wroblewski, P.: ApJ **712**, 964 (2010)
33. Güver, T., Wroblewski, P., Camarota, L., Özel, F.: ApJ **719**, 1807 (2010)
34. Özel, F., Gould, A., Güver, T.: ApJ **748**, 5 (2012)
35. Güver, T., Özel, F.: ApJ **765**, 1 (2013)

36. Guillot, S., Servillat, M., Webb, N.A., Rutledge, R.E.: ApJ **772**, 7 (2013)
37. Dickey, J.M., Lockman, F.J.: Annu. Rev. Ast. Ap. **28**, 215 (1990)
38. Steiner, A.W., Lattimer, J.M., Brown, E.F.: ApJ **765**, 43 (2013)
39. Suleimanov, V., Poutanen, J., Werner, K.: Astron. Astrophys. **527**, A139 (2011)
40. Gendreau, K., Arzoumanian, Z., Okajima, T.: SPIE **8443**, 844313 (2012)
41. Feroci, M., et al.: Exp. Ast. **34**, 415 (2012)
42. Leahy, D.A., Morsink, S.M., Chou, Y.: ApJ **742**, 17 (2011)
43. Lyne, A.G., et al.: Science **303**, 1153 (2004)
44. Lattimer, J.M., Schutz, B.F.: ApJ **629**, 979 (2005)
45. Link, B., Epstein, R.I., Lattimer, J.M.: Phys. Rev. Lett. **83**, 3362 (1999)